




Relaminarization of elastic turbulence

M. Vijay Kumar ^{1,2,3,*}, Atul Varshney ^{1,4,5,*}, Dongyang Li,^{1,6} and Victor Steinberg ^{1,2}

¹*Department of Physics of Complex Systems, Weizmann Institute of Science, Rehovot 76100, Israel*

²*The Racah Institute of Physics, Hebrew University of Jerusalem, Jerusalem 91904, Israel*

³*Department of Mechanical and Industrial Engineering, University of Illinois at Chicago, Chicago, Illinois 60607, USA*

⁴*School of Physical Sciences, National Institute of Science Education and Research, HBNI, Jatni-752050, Odisha, India*

⁵*Institute of Science and Technology Austria, Am Campus 1, 3400 Klosterneuburg, Austria*

⁶*College of Nuclear Science and Technology, Harbin Engineering University, Harbin 150001, China*



(Received 30 October 2021; accepted 22 July 2022; published 3 August 2022)

We report frictional drag reduction and a complete flow relaminarization of elastic turbulence (ET) at vanishing inertia in a viscoelastic channel flow past an obstacle. We show that the intensity of the observed elastic waves and wall-normal vorticity correlate well with the measured drag above the onset of ET. Moreover, we find that the elastic wave frequency grows with the Weissenberg number, and at sufficiently high frequency it causes a decay of the elastic waves, resulting in ET attenuation and drag reduction. Thus, this allows us to substantiate a physical mechanism, involving the interaction of elastic waves with wall-normal vorticity fluctuations, leading to the drag reduction and relaminarization phenomena at low Reynolds number.

DOI: [10.1103/PhysRevFluids.7.L081301](https://doi.org/10.1103/PhysRevFluids.7.L081301)

Curvilinear flows of dilute polymer solution exhibit elastic instabilities and elastic turbulence (ET) at vanishing inertia. ET is a spatially smooth and temporally random flow, characterized by a strong enhancement of a flow resistance, a steep power-law decay of the velocity power spectrum with an exponent $|\alpha| > 3$ indicating that only a few modes are relevant to flow dynamics, and an orders-of-magnitude enhancement of mixing compared with diffusion [1,2]. In such flows, the elastic stress generated by polymer stretching along curved streamlines initiates a backreaction on the flow in the curvature direction and triggers a linear normal mode elastic instability and ET at $Wi \gg 1$ and $Re \ll 1$ [1,2]. However, this instability mechanism becomes ineffective in zero curvature parallel shear flows, such as pipe, channel, and plane Couette [1–6]. Here, the degree of polymer stretching [7] is defined by the Weissenberg number $Wi = \lambda U/d$ and the ratio of inertial and viscous stresses by the Reynolds number $Re = \rho U d/\eta$; U is the mean fluid speed, λ is the longest polymer relaxation time, η and ρ are the solution viscosity and density, respectively, and d is the characteristic vessel size.

The first signature of a linear elastic instability was reported in a viscoelastic channel flow obstructed by two widely spaced obstacles [6]. The linear Hopf instability occurs due to a breaking of time-reversal symmetry leading to spanwise oscillations of a pair of eddies. Further, two shear (mixing) layers with zero curvature streamlines are generated due to the vortex pair elongation with Wi [8]. It follows by a secondary transition directly to ET and elastic waves at $Re \ll 1$ [8–10]. The measured friction factor f/f_{lam} as a function of Wi exhibits distinct scaling exponents in three flow

*These authors contributed equally to this work.

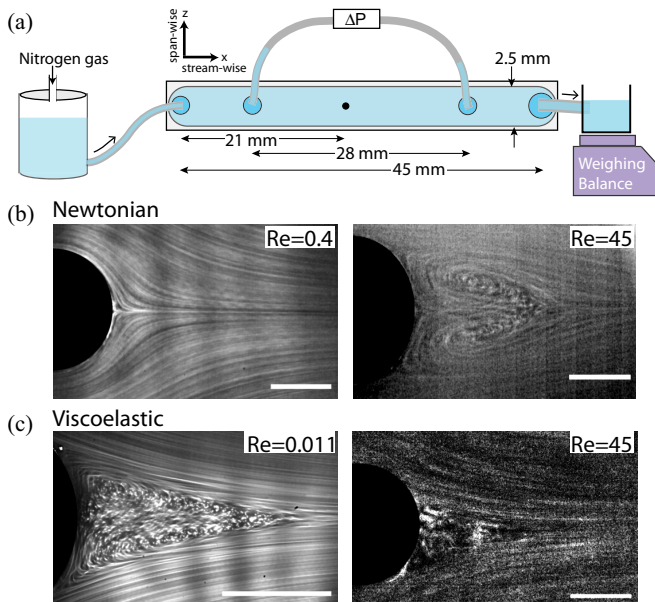


FIG. 1. (a) Schematic of the experimental setup (not to scale). Long-exposure particle streak images of the flow in the wake of the cylinder for (b) Newtonian fluid at $Re = 0.4$ and 45 , and (c) viscoelastic fluid at $(Re, Wi, El) = (0.011, 312, 28\,251)$ and $(45, 492, 11)$. The scale bars are $150\ \mu\text{m}$. The flow direction is from left to right.

regimes: $Wi^{0.5}$ (transition), $Wi^{0.2}$ (ET), and $Wi^{-0.2}$ [drag reduction (DR)] [6,8,9]. Here, f_{lam} is the friction factor for laminar flow. Remarkably, the extent of DR was reduced either with decreasing fluid elasticity $El (= Wi/Re)$ or increasing inertia (or Re), while flow relaminarization was found at $El \geq 1000$ and $Re < 10$ [9]. It should be emphasized that both elastic waves and DR down to relaminarization were observed only in a viscoelastic channel flow in a chaotic regime [9–11].

On the other hand, an addition of a minute amount of long-chain flexible polymers in high- Re shear flows causes a suppression of small-scale turbulent structures and reduces frictional drag up to 80%, known as the turbulent drag reduction (TDR) phenomenon [12]. Here, both the inertia and elastic stresses, and their interplay contribute to the mechanism of TDR [13]. However, the DR and relaminarization at $Re \ll 1$ (described above) occur in channel flows only due to the elastic stress engendered at negligible inertia [9,11], and they significantly differ from TDR occurring at $Re \gg 1$ [12,13].

In this Letter we report a key mechanism of DR and relaminarization at vanishing inertia, observed first in Ref. [9]. We find a good correlation between elastic wave intensity I , wall-normal vorticity fluctuations, and flow resistance in a viscoelastic flow past an obstacle, where I is considered as the key factor in the suggested amplification mechanism by elastic waves. Further, we demonstrate that increasing frequency of elastic waves with Wi results in their strong attenuation that hinders ET growth and leads to DR. We believe that this mechanism is generic to viscoelastic parallel shear flows, in which elastic waves appear.

The experiments are conducted in a straight channel of dimensions $L \times w \times h = 45 \times 2.5 \times 1\ \text{mm}^3$ made of transparent acrylic glass and with an obstacle of $d = 0.3\ \text{mm}$ at its center [Fig. 1(a)]. The fluid is driven by N_2 gas at a pressure up to ~ 60 psi and injected at the inlet. As a working fluid, a dilute polymer solution of high molecular weight M_w polyacrylamide ($M_w = 18\ \text{MDa}$; Polysciences) at a concentration $c = 80\ \text{ppm}$ ($c/c^* \approx 0.4$, where $c^* \approx 200\ \text{ppm}$ is the overlap polymer concentration [14]), is prepared using water-sucrose solvent with sucrose from 0 to 65%

weight fraction. Due to the addition of polymers to the solvent, the solution viscosity η increases about 30%. The solvent viscosity η_s is measured by a rheometer (AR-1000; TA Instruments) at 20 °C. For $\eta_s = 100$ mPa s solution, one gets $\lambda = 10 \pm 0.2$ s, obtained by the stress-relaxation method [14]. The latter depends linearly on η_s [14]. The polymer solution properties for four El are presented in Supplemental Table S1 [15].

High-sensitivity ($\pm 0.25\%$ of full scale) differential pressure sensors (HSC series, Honeywell) of different ranges are used to measure the pressure drop ΔP across the obstacle at a separation $L_c = 28$ mm. The exiting fluid is weighed instantaneously $W(t)$ as a function of time by a computer-interfaced balance (BA210S, Sartorius). The time-averaged fluid discharge rate $\bar{Q} = \overline{\Delta W / \Delta t}$ is used to get the mean velocity $U = \bar{Q} / \rho wh$.

For streak flow visualization and microscale particle image velocimetry (μ PIV) measurements via a microscope (Olympus IX70), the solution is seeded with fluorescent particles of diameter 1 μ m (Fluoresbrite YG, Polysciences). A high-speed camera (FASTCAM Mini WX100, Photron) with a spatial resolution 2048×2048 pixels at a rate of 50 fps is used. The flow in the wake is illuminated by a thin sheet laser (447.5 nm) beam via the telescope arrangement. Microscope objectives, $10\times$ for El = 11 and $20\times$ for the rest of El, are used. For μ PIV measurements, images are acquired with low and high spatial resolutions for temporal velocity power spectra and flow structures, respectively. The fast Fourier transform (FFT)-based correlation [16] with 32×32 px box size corresponding to $18.8 \times 18.8 \mu\text{m}^2$ (at $10\times$) and $10.6 \times 10.6 \mu\text{m}^2$ (at $20\times$) and with each box having at least 5–10 particles.

A striking difference in the flow dynamics of Newtonian and viscoelastic fluids in the cylinder wake is illustrated via the streak flow images in Figs. 1(b) and 1(c), respectively. For Newtonian fluid in the Stokes limit ($\text{Re} = 0.4$), the flow is laminar [Fig. 1(b) left]. Above $\text{Re} \sim 20$, a boundary layer commences to separate from the cylinder surface leading to a pair of steady eddies attached to the cylinder at $\text{Re} \sim 40$, and further to an oscillating vortex pair shown at $\text{Re} = 45$ in Fig. 1(b) right.

On the other hand, flow of a viscoelastic fluid exhibits the linear elastic instability at Wi_c and $\text{Re} \approx 0.005$. At higher Wi , ET arises [4,6,17]. Around the onset of ET, fluctuating wall-normal vortices appear in the downstream wake at $\text{Re} = 0.011$, $\text{Wi} = 312$ for El = 28 251 [Fig. 1(c) left], contributing to an increase of f/f_{lam} . At $\text{Re} \gg 1$, an interplay of inertial and elastic stresses can lead to a suppression of small-scale vortices for El $\sim O(1)$ and thereby to a reduction of the frictional drag [18] leading to the TDR regime [12,13]. In contrast, in Fig. 1(c) right, the visible suppression of small-scale fluctuating vortices in a viscoelastic flow takes place at $\text{Re} = 45$, $\text{Wi} = 492$ (El = 11), deep in the DR regime that can be compared with the Newtonian case at the same Re [Fig. 1(b) right]. In this case, the inertial stress is still significantly smaller than the elastic one, meaning that the DR as well as relaminarization phenomena are solely governed by the elastic stress.

A detailed demonstration of the flow structures in all three flow regimes—transition, ET, and DR—is presented in Fig. 2 at various (Re, Wi, El). In Fig. 2(a), we show the evolution of the flow regimes as a function of Re and Wi while keeping El = 28 251 fixed. At $\text{Wi} = 1.83$ and $\text{Wi} = 38.6$ (first two images), the flow structures of potential and weakly perturbed laminar flow in the vicinity of the obstacle are shown, respectively. With a further increase of (Re, Wi), flow becomes irregular, exhibiting ET, which subsequently weakens at higher (Re, Wi) leading to DR [6,17]. At El = 28 251, the transition to ET appears at $\text{Wi} \sim 360$ [Fig. 1(c)] leading to the growth of fluctuating vortices, and the vortex dynamics becomes more vigorous up to $\text{Wi} = 1050$, at which the ET-DR transition takes place. At further Wi increase, the vortex dynamics slows down and small-scale vortices are progressively suppressed leading to a smoother spatial scale and DR. For instance, the unsteady flow structures are constricted only in the proximity of the wake ($\sim 0.2d$) at $\text{Re} = 0.14$ and $\text{Wi} = 4035$, contrary to structures spanning up to the obstacle size at $\text{Wi} = 312$ [Fig. 2(a)].

We perform the measurements of the friction factor as a function of Wi for four El values, calculated as $f = 2\Delta P D_h / \rho L_c U^2$ and normalized by $f_{\text{lam}} \sim \text{Re}^{-1}$ (see Supplemental Fig. S1 [15]). Here, $D_h = 2wh/(w+h) = 1.43$ mm is the hydraulic radius [6]. The elastic transition is evident on a high-resolution plot by the exponent 0.5 in f/f_{lam} vs Wi (Fig. 3). The changes of f/f_{lam} with

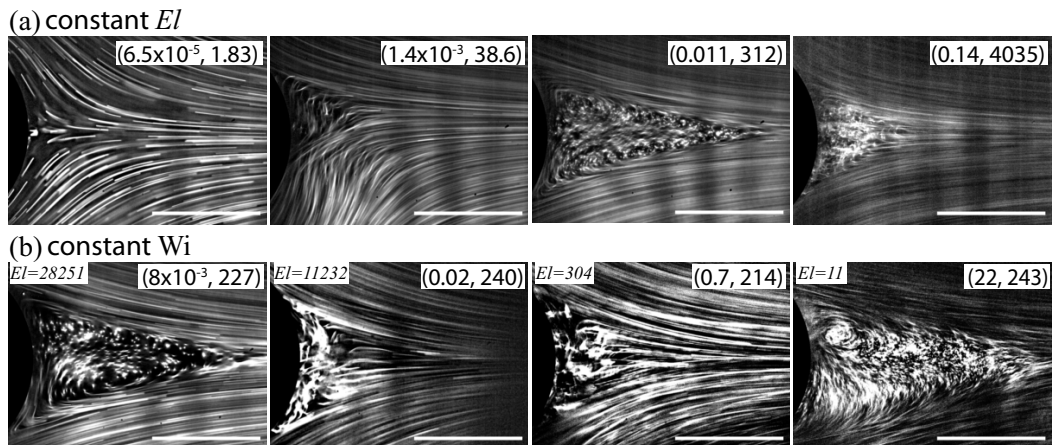


FIG. 2. Particle streak flow images of the wake at various (Re, Wi) and El . Evolution of flow structures in the wake of the cylinder: (a) at constant $El \sim 28251$ and (b) at nearly constant $Wi \approx 230 \pm 7\%$, and for different Re and El values. The scale bars are $150 \mu m$. The flow direction is from left to right.

Wi are qualitatively similar for all El : The transition and ET regimes show a drag enhancement, followed by a decrease of f/f_{lam} with increasing Wi , indicating the transition to DR. Further, the scaling exponents of the f/f_{lam} on Wi above the secondary instability (Fig. 3) are approximately the same at all El , i.e., $Wi^{0.2 \pm 0.04}$ and $Wi^{-0.18 \pm 0.05}$ for ET and DR, respectively. The exponent 0.2 in ET is close to the values found in various configurations of channel flow with and without perturbations [11, 19, 20]. Obviously, the linear elastic instability, ET, and DR occur at different Wi and Re for four El (Fig. 3 and in Supplemental Table S1 [15]). For Newtonian fluid, a drag enhancement begins at $Re \approx 35$ [Supplemental Fig. S1 and Fig. 1(b)]. Strikingly, for the high elasticity fluids ($El = 11, 232$ and $28, 251$), the drag reduction continues until the flow relaminarizes, i.e., f/f_{lam} returns back to the laminar value at $(Re, Wi) \approx (0.35, 4000)$ and $(0.27, 7627)$, respectively. The transition value from ET to DR for each El , marked by the arrow in Fig. 3, is determined by a slope sign change from positive to negative in f/f_{lam} vs Wi . The transition value of Wi for each El is tabulated in Supplemental Table S1 [15]. Moreover, the observations of flow structures via streak images in Fig. 2 corroborate well with the dependence of f/f_{lam} on Wi for $El = 28251$ (Fig. 3).

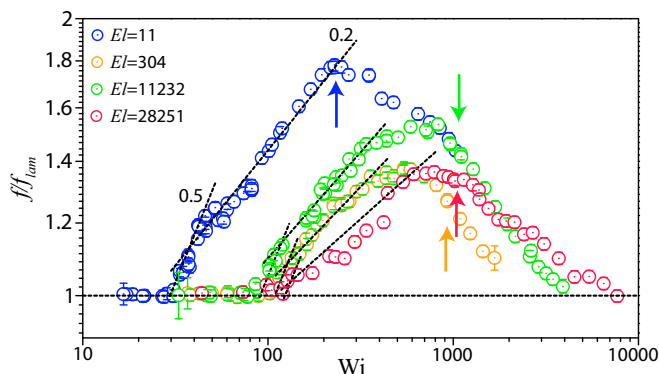


FIG. 3. Normalized friction factor f/f_{lam} vs Wi for four El . Dashed lines are fits with an exponent value of 0.5 and 0.2 in the elastic instability and ET regimes, respectively. Arrows indicate ET-to-DR transitions.

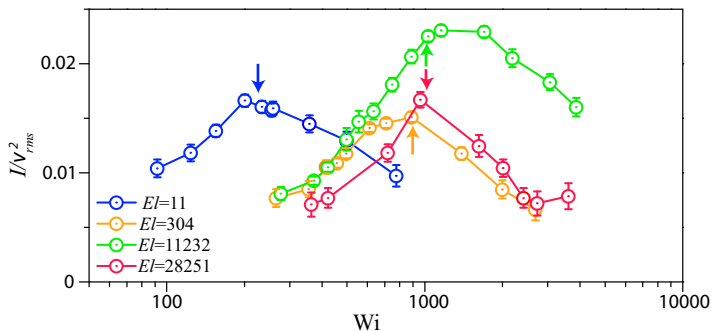


FIG. 4. Normalized intensity of elastic waves (I/v_{rms}^2) vs Wi . Arrows indicate the location of the ET-to-DR transition, obtained from f/f_{lam} vs Wi in Fig. 3.

Next, we unravel the role of elastic and inertial stresses in flow structures that lead to a nonmonotonic dependence of f/f_{lam} on Wi in Fig. 3. Similarly, the role of inertia in the presence of an elastic stress field is explored by varying Re from low to moderate values, while maintaining Wi nearly constant ($\approx 230 \pm 7\%$), as shown in Fig. 2(b). We achieve this goal for the fluids with different El . In the limit of vanishing Re and $Wi \gg 1$, the elastic Hopf instability occurs in the form of oscillating vortices, as shown at $Wi = 227$ [Fig. 2(b), first image], whereas at $Wi \approx 360$, corresponding to ET, fluctuating wall-normal vortices are found. At $Re = 0.02$ and $El = 11\,232$, the spatial extent of the vortical structure declines and confines narrowly to the obstacle [Fig. 2(b), second image]. At further increase in $Re = 0.7$ ($El = 304$), the extent of fluctuating vortices expands again in the wake [Fig. 2(b), third image]. And finally at $Re = 22$ and $El = 11$, the extent of turbulent eddies grows, filling the expanding downstream wake [Fig. 2(b), fourth image]. However, the nonmonotonic variations in structure dynamics and wake extent, at nearly the same Wi and increasing Re , are predominantly due to the elastic stress, since inertial effects are much less significant.

Elastic waves are nondispersive with the wave speed depending on stress instead of elasticity of the medium, analogous to the Alfvén wave in plasma [10]. To excite either Alfvén or elastic waves the perturbations should be transverse to the propagation direction. The elastic wave intensity [peak height in the velocity spectrum $S(v)$] plays a key role in giving rise to ET and DR [21]. We perform μ PIV measurements of span- and streamwise velocity fields in a wide range of Wi . From the peaks in spanwise velocity spectra shown in linear and logarithmic coordinates (see the typical spectra for $El = 11\,232$ in Supplemental Fig. S2 [15]), we obtain the dependence of the normalized elastic wave intensity I/v_{rms}^2 (Fig. 4) and frequency ν_{el} [Fig. 6(a)] on Wi in both ET and DR. Here, v_{rms} are the rms fluctuations of spanwise velocity. The dependence of I/v_{rms}^2 on Wi is shown in Fig. 4; I/v_{rms}^2 grows with Wi in the ET regime and decreases in DR for all El . In both the ET and DR regimes, the dependency of I/v_{rms}^2 on Wi shows a power-law behavior (Supplemental Fig. S3 [15]). To show the correlation between frictional drag and elastic wave intensity, we plot f/f_{lam} (Fig. 3) against I/v_{rms}^2 (Fig. 4) at nearly the same Wi in both ET and DR regimes for all El [Figs. 5(a) and 5(b)]. The linear dependence of f/f_{lam} on I/v_{rms}^2 indicates an excellent correlation in the growth of the friction factor and intensity of elastic waves in ET and their decay in DR and relaminarization. Also, wall-normal vorticities in the streak flow images agree well with the observed correlation in both regimes [Figs. 1(b) and 2(a) at $El = 28\,251$].

Further, we estimate the wave number (k_{el}) of the elastic waves using ν_{el} and the elastic wave speed (c_{el}) given in Ref. [10]; their dependencies on Wi are shown in Fig. 6. The elastic wave frequency ν_{el} grows nonmonotonically up to two orders of magnitude with Wi [Fig. 6(a)], however, the wave number k_{el} does not vary substantially, particularly in DR [Fig. 6(b)]. Elastic wave intensity and its frequency and wave number show reasonable agreement on the ET-DR transition Wi values for all El (see Supplemental Fig. S4 [15]). The elastic instability threshold Wi_c , and the onset Wi values for ET and DR at each El are tabulated in Supplemental Table S1 [15].

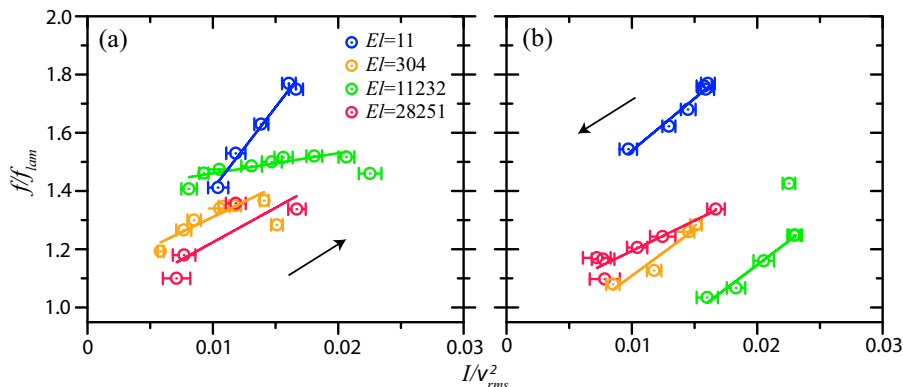


FIG. 5. Correlation between the friction factor and normalized elastic wave intensity in (a) ET and (b) DR regimes for various El . Solid lines are linear fits to the data. Arrows indicate the direction of increasing Wi .

A similar agreement is observed in two additional analyses: geometrical characterization of the wake (Supplemental Fig. S5 [15]), v_{rms}^2 (Supplemental Fig. S6(a) [15]), and the dependence of f/f_{lam} on v_{rms}^2 [Supplemental Figs. S6(b) and S6(c)]. We compute both the surface area (A) and length (l) of the wake from the streak images as a function of Wi for all values of El . Supplemental Fig. S5 [15] shows a normalized area ($4A/\pi d^2$) and length (l/d) of the wake versus $Wi - Wi_c$. Above the instability $Wi > Wi_c$, the wake grows up to the ET-DR transition, resulting in an increase of A and l with Wi , whereas beyond the ET-DR transition, both A and l decrease with Wi . In Supplemental Fig. S6 [15], analogous changes in v_{rms}^2 behavior with Wi are observed. These observations corroborate well with f/f_{lam} [Fig. 3 and Supplemental Figs. S6(b) and S6(c)].

The main observation for understanding the mechanism of the ET attenuation leading to DR and relaminarization is an excellent correlation between f/f_{lam} and I/v_{rms}^2 (Fig. 5). Indeed, the larger (smaller) f/f_{lam} , the greater (smaller) I/v_{rms}^2 , and I/v_{rms}^2 tends to zero at relaminarization, quantified in their dependence in Fig. 5. Thus, the observed correlation between the frictional drag and elastic wave intensity suggests the following plausible mechanism of ET suppression resulting in DR and relaminarization.

A synchronous interaction of the elastic waves with wall-normal vorticity fluctuations leads to their amplification in ET and subsequent suppression in DR. This mechanism of the resonant interaction results in an effective energy pumping from the elastic waves to wall-normal vortices.

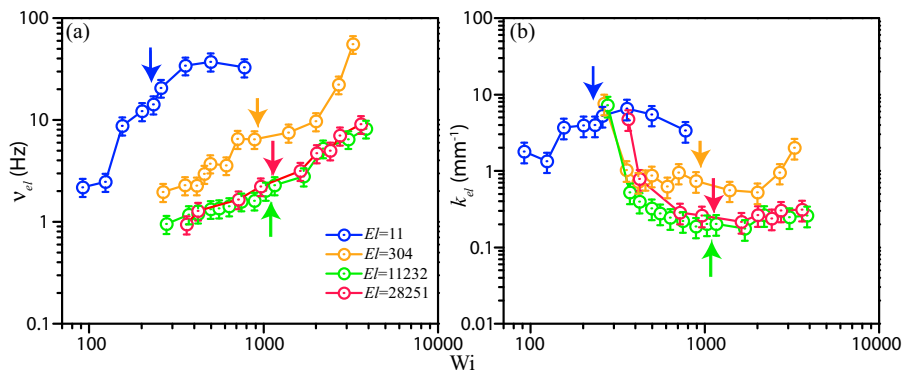


FIG. 6. Dependence of (a) frequency ν_{el} and (b) wave number k_{el} of elastic waves on Wi for different El . Arrows indicate the location of the ET-to-DR transition, obtained from f/f_{lam} vs Wi in Fig. 3.

The physics of the interaction of the elastic waves with fluctuating vortices is analogous to the Landau wave damping [22], occurring due to the resonant interaction of electromagnetic waves with electrons in plasma, when the electron velocity coincides with the wave phase speed. Similarly, acoustic damping occurs in the sound-gas bubble interaction [23], resulting in strong wave attenuation. It is also similar to the amplification mechanism of wall-normal fluctuating vortices by the elastic waves in an elastically driven Kelvin-Helmholtz-like instability [24]. Then an increase of the wall-normal vorticity results in f/f_{lam} growth at increasing I/v_{rms}^2 in ET and its reduction at diminishing I/v_{rms}^2 in the DR regime.

Then a further question arises: What causes a drastic change from I/v_{rms}^2 growth in ET to its decrease in DR? We suggest that the main reason is the increase in elastic wave dissipation [21] due to increasing ν_{el} . Indeed, there are two plausible mechanisms of the elastic wave attenuation: the elastic stress relaxation limiting the range of elastic wave existence at low k_{el} or low ν_{el} , and viscous dissipation [21] restricting from high k_{el} or high ν_{el} . The former has a scale-independent attenuation, which at low values satisfies the relation $\lambda\omega > 1$, whereas the latter provides low attenuation at high ν_{el} via the inequality $\omega \geq \eta k_{\text{el}}^2/\rho$, where $\omega = 2\pi\nu_{\text{el}}$. Using both inequalities, one gets the range of low dissipation of the elastic waves, which by substitution $\omega = c_{\text{el}}k_{\text{el}}$ leads to $\sim 10^{-2} < \nu_{\text{el}} < \rho c_{\text{el}}^2/2\pi\eta$ at $c_{\text{el}} = 0.5 \times 10^{-3}(\text{Wi} - \text{Wi}_c)^{0.73}$ m/s for $\text{El} = 11\,232$ (similar estimates can be made for other El) [10]. From the second part of the inequality, one finds that the low dissipation range of the elastic waves collapses at $\text{Wi}_{\text{ET-DR}} = 1030$ for f/f_{lam} (Fig. 3) and I/v_{rms}^2 (Fig. 4) that occurs at approximately $\nu_{\text{el}} \geq 8$ Hz. It is larger than the experimental value of ≈ 2 Hz [Fig. 6(a)] because of additional elastic wave damping due to resonant interaction with the wall-normal fluctuating vortices explained above. Thus, the collapse of the low dissipation range of the elastic waves and so the appearance of large attenuation is the reason for the emergence of the DR regime.

In summary, our experiments suggest the physical origin of the existence of DR and relaminarization at $\text{Re} \ll 1$. The correlation of the frictional drag with elastic wave intensity, and wall-normal vorticity observed in the ET and DR regimes, indicate that the interaction of the elastic waves with fluctuating wall-normal vortices leads to either their amplification or attenuation. Thus, the larger (smaller) elastic wave intensity, the larger (smaller) the frictional drag, which explains the appearance of DR at $\text{Re} \ll 1$.

We thank G. Falkovich for discussion and Guy Han for technical support. We are grateful to N. Jha for his help in μPIV measurements. This work is partially supported by the grants from Israel Science Foundation (ISF Grants No. 882/15 and No. 784/19) and Binational U.S.-Israel Foundation (BSF Grant No. 2016145).

-
- [1] V. Steinberg, Elastic turbulence: An experimental view on inertialess random flow, *Annu. Rev. Fluid Mech.* **53**, 27 (2021).
 - [2] A. Groisman and V. Steinberg, Elastic turbulence in a polymer solution flow, *Nature (London)* **405**, 53 (2000).
 - [3] R. G. Larson, Instabilities in viscoelastic flows, *Rheol. Acta* **31**, 213 (1992).
 - [4] E. S. G. Shaqfeh, Purely elastic instabilities in viscometric flows, *Annu. Rev. Fluid Mech.* **28**, 129 (1996).
 - [5] P. Pakdel and G. H. McKinley, Elastic Instability and Curved Streamlines, *Phys. Rev. Lett.* **77**, 2459 (1996).
 - [6] A. Varshney and V. Steinberg, Elastic wake instabilities in a creeping flow between two obstacles, *Phys. Rev. Fluids* **2**, 051301(R) (2017).
 - [7] R. B. Bird and O. Hassager, *Dynamics of Polymeric Liquids: Fluid Mechanics* (Wiley, New York, 1987), Vols. 1 and 2.
 - [8] A. Varshney and V. Steinberg, Mixing layer instability and vorticity amplification in a creeping viscoelastic flow, *Phys. Rev. Fluids* **3**, 103303 (2018).

- [9] A. Varshney and V. Steinberg, Drag enhancement and drag reduction in viscoelastic flow, *Phys. Rev. Fluids* **3**, 103302 (2018).
- [10] A. Varshney and V. Steinberg, Elastic Alfven waves in elastic turbulence, *Nat. Commun.* **10**, 652 (2019).
- [11] N. K. Jha and V. Steinberg, Universal coherent structures of elastic turbulence in straight channel with viscoelastic fluid flow, [arXiv:2009.12258](https://arxiv.org/abs/2009.12258).
- [12] P. S. Virk, Drag reduction fundamentals, *AIChE J.* **21**, 625 (1975).
- [13] K. R. Sreenivasan and C. M. White, The onset of drag reduction by dilute polymer additives, and the maximum drag reduction asymptote, *J. Fluid Mech.* **409**, 149 (2000).
- [14] Y. Liu, Y. Jun, and V. Steinberg, Concentration dependence of the longest relaxation times of dilute and semi-dilute polymer solutions, *J. Rheol.* **53**, 1069 (2009).
- [15] See Supplemental Material at <http://link.aps.org/supplemental/10.1103/PhysRevFluids.7.L081301> for properties of dilute polymer solution used and additional figures.
- [16] W. Thielicke and E. J. Stamhuis, PIVlab—Towards user-friendly, affordable and accurate digital particle image velocimetry in MATLAB, *J. Open Res. Softw.* **2**, e30 (2014).
- [17] M. Grilli, A. Vázquez-Quesada, and M. Ellero, Transition to Turbulence and Mixing in a Viscoelastic Fluid Flowing Inside a Channel with a Periodic Array of Cylindrical Obstacles, *Phys. Rev. Lett.* **110**, 174501 (2013).
- [18] K. P. Nolan, A. Agarwal, S. Lei, and R. Shields, Viscoelastic flow in an obstructed microchannel at high Weissenberg number, *Microfluid. Nanofluid.* **20**, 101 (2016).
- [19] Y. Li and V. Steinberg, Universality in the properties and structures of viscoelastic channel flows with weak and strong perturbations, [arXiv:2201.06342](https://arxiv.org/abs/2201.06342).
- [20] V. Steinberg, New direction and perspectives in elastic instability and turbulence in various viscoelastic flow geometries without inertia (short review), *Low Temp. Phys.* **48**, 492 (2022).
- [21] E. Balkovsky, A. Fouxon, and V. Lebedev, Turbulence of polymer solutions, *Phys. Rev. E* **64**, 056301 (2001).
- [22] 61: On the vibrations of the electronic plasma, in *Collected Papers of L. D. Landau*, edited by D. ter Haar (Pergamon Press, Oxford, UK, 1965), pp. 445–460.
- [23] D. D. Ryutov, Analog of Landau damping the problem of sound-wave propagation in a liquid with gas bubbles, *Pis'ma Zh. Eksp. Teor. Fiz.* **22**, 446 (1975).
- [24] N. K. Jha and V. Steinberg, Elastically driven Kelvin-Helmholtz-like instability in straight channel flow, *Proc. Natl. Acad. Sci. USA* **118**, e2105211118 (2021).